Acta Geotechnica (2021) 16:4007–4026
https://doi.org/10.1007/s11440-021-01344-0

RESEARCH PAPER

# An approach for modelling spatial variability in permeability of cement-admixed soil

Hardy Yide Kek[1] · Yutao Pan[2] · Yannick Choy Hing Ng[1] · Fook Hou Lee[1]

Received: 22 February 2021 / Accepted: 22 August 2021 / Published online: 8 September 2021


## Abstract

This paper presents a framework for modelling the random variation in permeability in cement-admixed soil based on the binder content variation and thereby relating the coefficient of permeability to the unconfined compressive strength of a cement-admixed clay. The strength–permeability relationship was subsequently implemented in random finite element method (RFEM). The effects of spatial variation in both strength and permeability of cement-admixed clays in RFEM is illustrated using two examples concerning one-dimensional consolidation. Parametric studies considering different coefficient of variation and scale of fluctuation configurations were performed. Results show that spatial variability of the cement-admixed clay considering variable permeability can significantly influence the overall consolidation rate, especially when the soil strength variability is high. However, the overall consolidation rates also depend largely on the prescribed scales of fluctuation; in cases where the variation is horizontally layered, stagnation in pore pressure dissipation may occur due to soft parts yielding.

**Keywords** Consolidation · Cement stabilisation · Permeability · Random finite element · Spatial variability

**Abbreviations**

| | |
|---|---|
| $x$ | Soil-cement ratio of mix |
| $y$ | Water-cement ratio of mix |
| $b$ | Binder mass fraction |
| $w_i$ | In-situ water content |
| $a$ | Water-cement ratio of cement slurry |
| $A_w$ | Cement content |
| $e_i$ | As-mixed void ratio |
| $R_{\mathrm{wt}}$ | Mass fraction of water in mix |
| $R_{\mathrm{s}}$ | Mass fraction of soil solids in mix |
| $R_{\mathrm{c}}$ | Mass fraction of cement solids in mix |
| $G_{\mathrm{s}}$ | Specific gravity of soil solids |
| $G_{\mathrm{c}}$ | Specific gravity of cement solids |
| $m_{\mathrm{c}}$ | Post-curing mass of cementitious solids |
| $m_{\mathrm{cement}}$ | Mass of cement solids before curing |
| $h_t$ | Degree of hydration |
| $\beta_1$ | Mass ratio of hydrated water to dry cement solids |
| $V_{\mathrm{c}}$ | Volume of cementitious solids |
| $\gamma_{\mathrm{w}}$ | Unit weight of water |
| $\eta$ | Volume ratio of hydrated products |
| $V_{1,\mathrm{d}}$ | Volume of water after drained curing |
| $e_{\mathrm{d}}$ | Void ratio under drained curing conditions |
| $e_{\mathrm{u}}$ | Void ratio under undrained curing conditions |
| $e_0$ | Post-curing void ratio |
| $k$ | Coefficient of permeability |
| $x_1$ | Constant |
| $x_2$ | Constant |
| $q_u$/UCS | Unconfined compressive strength |
| $r$ | Strength ratio |
| $q_0$ | Fitting parameter |
| $m$ | Fitting parameter |
| $n$ | Fitting parameter |
| $C_{\mathrm{w}}$ | Total water content of mix |
| $C_m$ | Cement amount |

✉ Yutao Pan
yutao.pan@ntnu.no

Hardy Yide Kek
hardykek@u.nus.edu

Yannick Choy Hing Ng
yannick_ng@nus.edu.sg

Fook Hou Lee
leefookhou@nus.edu.sg

[1] Department of Civil and Environmental Engineering, National University of Singapore, 1 Engineering Drive 2, Singapore 117576, Singapore

[2] Department of Civil and Environmental Engineering, Norwegian University of Science and Technology, Høgskoleringen 7a, Gløshaugen, Norway

| | |
|---|---|
| $D$ | Model height |
| $W$ | Model width |
| COV | Coefficient of variation |
| SOF | Scale of fluctuation |
| $m_v$ | Coefficient of volume compressibility |
| $\overline{U}$ | Average degree of consolidation |
| $c_{v,eq}$ | Equivalent coefficient of consolidation |
| $H_d$ | Drainage path length |
| $t_{90}$ | Duration corresponding to 90% ultimate consolidation settlement |
| $t_{50}$ | Duration corresponding to 50% ultimate consolidation settlement |
| $\overline{\kappa}$ | Modified swelling index |
| $\lambda_r$ | Compression index of remoulded cement-admixed clay |
| $M$ | Friction coefficient |
| $\alpha$ | Isotropic degradation parameter |
| $\beta$ | Cohesion degradation parameter |
| $\nu'$ | Effective Poisson's ratio |
| $V_0$ | Initial specific volume |
| $\sigma_t$ | Tensile strength |
| $p'_{py}$ | Primary yield stress |
| $C_i$ | Initial cohesion |
| $t$ | Time duration |
| $u_e$ | Excess pore pressure |
| $s$ | Settlement |
| $s_{ult}$ | Ultimate settlement |

## 1 Introduction

Cement admixture is commonly used for rapid improvement of soft clayey soils (e.g. [15, 18, 23, 36, 38, 49, 53, 56, 64]). An important issue with cement-admixed ground is its spatial variability (e.g. [2, 20, 21, 29]), which has been studied using random finite element method (RFEM) (e.g. [27, 33, 37–39]).

Liu et al. [27] studied the lateral compression of a spatially variable cement-admixed clay layer using three-dimensional (3D) RFEM, by considering the treated soil as a Tresca material. However, the total stress Tresca material cannot model the volumetric yielding and tensile failure of cement-admixed clays [59]. Pan et al. [37, 38] studied the effects of spatial variation in strength on the behaviour of axially loaded cement-admixed clay columns and laterally loaded cement-admixed clay slab under drained and undrained conditions using Xiao et al.'s [59] Cohesive Cam Clay (C3) material. The C3 material can capture the behaviour of cement-admixed clays over a large range of cement content, including tensile failure. The time-dependent behaviour of the cement-admixed clay was also investigated by Pan et al. [38]. However, these studies did not consider the spatial variation in permeability arising from the variation in cement and water contents in the treated soil, and its effect on the rate of pore pressure dissipation.

The permeability of a cement-admixed clay depends on its total water content, which is a proxy of its porosity [31]. However, for a fixed water content, the cement content is also known to significantly influence the permeability of the treated soil. Numerous studies have reported the decrease in permeability of the cement-admixed soil with increasing cement contents as well as curing duration (e.g. [22, 47, 57, 61]). This is attributable to the relationship between the treated clay permeability and its post-curing void ratio (e.g. [4, 31, 35, 42]), which is known to be affected by the amount of cementitious products (e.g. [16, 30]). However, Zhang et al.'s [63] data showed that higher strength and permeability are correlated with higher cement contents. This suggests that the relationship between strength and permeability for cement-admixed clays may not be monotonic, and a more thorough investigation is necessary.

Random finite element study on consolidation problems for soil with variable permeability and coefficient of volume change has been reported widely (e.g. [1, 3, 14]). However, the soil is assumed to behave in a linear elastic manner and does not undergo yielding. Moreover, Bari and Shahin's [1] study utilises only uncoupled flow deformation analyses. For settlement-sensitive infrastructures such as airport runways constructed over cement-admixed soil layers in the Hong Kong International Airport Expansion Project, the residual settlement is limited to 200 mm following surcharge removal [49]. An important parameter for predicting the time-dependent ground settlement is the consolidation settlement rate, which may be affected by spatial variability. However, to date, analytical and numerical studies involving realistic constitutive models with spatially variable permeability remain scarce.

This paper presents a framework for incorporating spatially variable permeability into RFEM of cement-admixed clays. The starting point is Chen et al.'s [2] study which relates the unconfined compressive strength of a cement-admixed clay to its cement slurry concentration and in-situ water content. Using Tyagi et al.'s [50] approach, the post-curing void ratio of the treated soil mass is deduced from the soil–cement–water mix proportion. The permeability is then deduced using previously published void ratio–permeability relationships [5, 31, 35, 42]. This allows the permeability to be related to the unconfined compressive strength. The strength–permeability relationship is then coded into the finite element software GeoFEA 9 (https://

www.geosoft.sg), where the variation in permeability can be specified as a random variable that is dependent upon the unconfined compressive strength. The methodology is illustrated using two examples to show the effect of random permeability on consolidation behaviour. In the second example, estimating the overall consolidation rate of the cement-admixed clay subgrade underlying airport runways [18, 49, 54] considering random permeability may be more representative of field conditions.

## 2 Method for evaluating spatially variable permeability

The approach adopted herein for evaluating spatially variable permeability consists of three steps. The post-curing void ratio of the cement-admixed clay is first related to its mix ratio, that is, the soil–cement and water–cement ratios at the point of mixing, using phase relationships. Using empirical relationships between the post-curing void ratio and permeability [5, 31, 35, 42], the latter is then related to the mix ratio. Finally, combining the results from parts (a) and (b) with Chen et al.'s [2] empirical relationship between unconfined compressive strength and mix ratio allows a relationship between permeability and unconfined compressive strength to be established. The flow chart for establishing the strength–permeability relationship is shown in Fig. 1. The governing equations for this approach are summarised below.

### 2.1 Void ratio of cement-admixed clay

Chen et al. [2] showed that the soil-cement ratio $x$ and water-cement ratio $y$ in the cement-admixed soil can be expressed as functions of the binder mass fraction $b$, in-situ water content $w_i$, and water-cement ratio of the binder $a$, by

$$x = \left(\frac{1+a}{1+w_i}\right)\left(\frac{1}{b}-1\right) \tag{1}$$

$$y = w_i x + a \tag{2}$$

An alternative definition is the cement content $A_w$, which is defined as the mass ratio of the cement solids to soil solids, i.e. $A_w = 1/x$ [30]. The void ratio of the cement-admixed soil at the point of mixing, termed hereafter as the as-mixed void ratio $e_i$, is given by Tyagi et al. [50]

$$e_i = \frac{R_{\mathrm{wt}}}{\left(\frac{R_{\mathrm{s}}}{G_{\mathrm{s}}}+\frac{R_{\mathrm{c}}}{G_{\mathrm{c}}}\right)} \tag{3}$$

where $G_{\mathrm{s}}$ and $G_{\mathrm{c}}$ are the specific gravities of the soil and cement solids, respectively, and $R_{\mathrm{wt}}$, $R_{\mathrm{s}}$, and $R_{\mathrm{c}}$ are the mass fractions of water, soil solids, and cement solids in

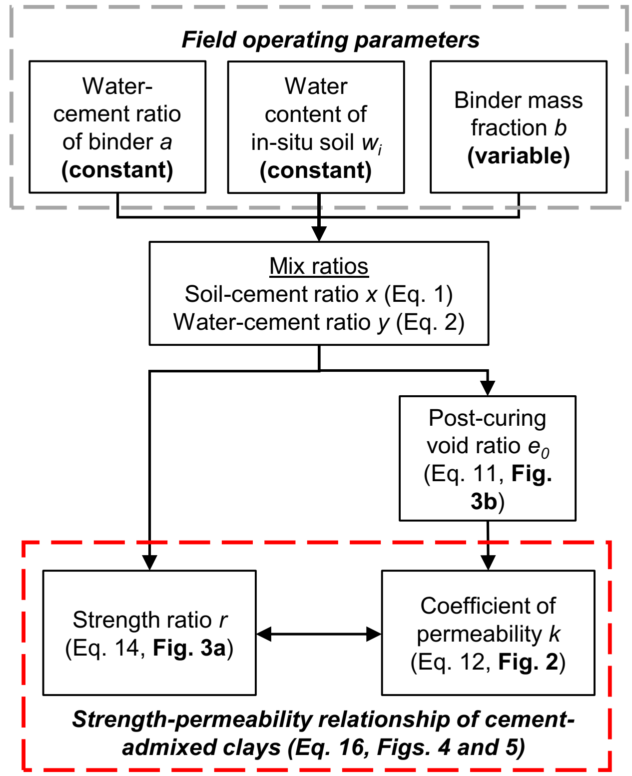


**Fig. 1** Flow chart for establishing the relationship between strength and permeability of cement-admixed clays

the cement-admixed soil, respectively. Based on the changes in constituents during cement hydration [34], Tyagi et al. [50] postulated that the post-curing mass of cementitious solids $m_c$ can be expressed as

$$m_{\mathrm{c}} = m_{\mathrm{cement}}(x + 1 + h_t\beta_1) \tag{4}$$

where $m_{\mathrm{cement}}$ is the mass of the cement solids before curing, $h_t$ the degree of hydration, and $\beta_1$ the mass ratio of the hydrated water to the anhydrous cement solids. The value of $h_t$ is 1 for the complete hydration of cement, and $\beta_1 \sim 0.23$, based on Neville's [34] observation that the net mass of water absorbed during the complete hydration reaction is about 0.23 times the mass of the anhydrous cement solids. Since the hydrated products occupy a volume smaller than the combined volumes of the anhydrous cement and the hydrated water by approximately 0.254 times the volume of the hydrated water [34], Tyagi et al. [50] proposed that the volume of cementitious solids produced during the hydration reaction $V_c$ can be expressed as

$$V_{\mathrm{c}} = \frac{m_{\mathrm{cement}}}{\gamma_{\mathrm{w}}}\left[\frac{x}{G_{\mathrm{s}}}+\frac{1}{G_{\mathrm{c}}}+(1-\eta)h_t\beta_1\right] \tag{5}$$

where $\gamma_w$ is the unit weight of water, and the parameter $\eta$ = 0.254.

Tyagi et al. [50] considered two extremes in curing conditions, namely drained and undrained curing. The drained curing condition assumes that the volume of the cement-soil admixture remains constant throughout the curing process, and changes in void ratio are accommodated by water ingress or egress. The undrained curing condition assumes that no water from the surrounding ingresses or egresses into the cement-soil admixture during the curing process, resulting in autogenous shrinkage of the cement-admixed soil.

Following Tyagi et al.'s [50] approach for the drained condition, the total volume of water post-curing $V_{1,d}$ and the corresponding void ratio $e_d$ are given by

$$V_{1,d} = \frac{m_{\text{cement}}}{\gamma_w}[y - (1-\eta)h_t\beta_1] \tag{6}$$

and

$$e_d = \frac{[y - (1-\eta)h_t\beta_1]}{\left[\frac{x}{G_s} + \frac{1}{G_c} + (1-\eta)h_t\beta_1\right]} \tag{7}$$

Substituting $\eta$ = 0.254 and $\beta_1$ = 0.23 into Eq. 7 gives

$$e_d = \frac{[y - 0.1716h_t]}{\left[\frac{x}{G_s} + \frac{1}{G_c} + 0.1716h_t\right]} \tag{8}$$

For undrained curing conditions, the corresponding void ratio $e_u$ can be expressed as

$$e_u = \frac{[y - 0.23h_t]}{\left[\frac{x}{G_s} + \frac{1}{G_c} + 0.1716h_t\right]} \tag{9}$$

Substituting Eqs. 1 and 2 into Eqs. 8 and 9 gives

$$e_d = \frac{w_i\left(\frac{1+a}{1+w_i}\right)\left(\frac{1}{b}-1\right) + a - 0.1716h_t}{\left(\frac{1}{G_s}\right)\left(\frac{1+a}{1+w_i}\right)\left(\frac{1}{b}-1\right) + \frac{1}{G_c} + 0.1716h_t} \tag{10}$$

$$e_u = \frac{w_i\left(\frac{1+a}{1+w_i}\right)\left(\frac{1}{b}-1\right) + a - 0.23h_t}{\left(\frac{1}{G_s}\right)\left(\frac{1+a}{1+w_i}\right)\left(\frac{1}{b}-1\right) + \frac{1}{G_c} + 0.1716h_t} \tag{11}$$

## 2.2 Void ratio–permeability relationship of cement-admixed clays

Fig. 2 presents the coefficient of permeability $k$ and the post-curing void ratio $e_0$ data of cement-admixed Ariake clays [35], Singapore marine clays [5], Bangkok soft clay [31], and Ariake clays and dredged muds [42]. The void ratio-permeability data are bounded by upper and lower limits, which can be approximated by the log-linear form

$$e_0 = x_1 \ln(k) + x_2 \tag{12}$$

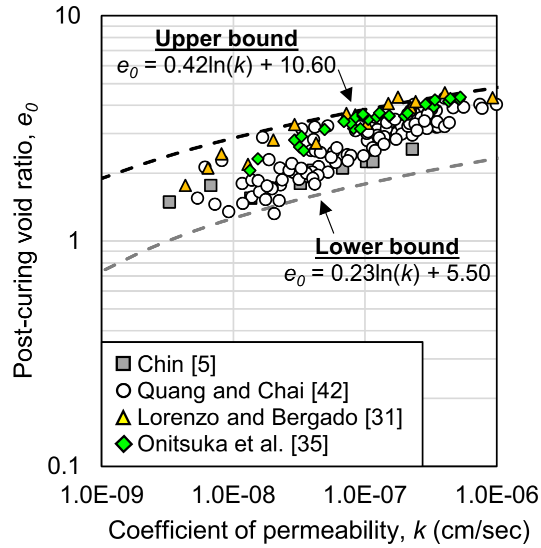


**Fig. 2** Void ratio-permeability relationship for cement-admixed clays from previously published literature

where the constants $x_1$ and $x_2$ represent the slope and the ordinate intercept of the permeability-void ratio plot, respectively. For the upper and lower bounds, the fitted values of $x_1$ are 0.42 and 0.23, respectively, while $x_2$ = 10.60 and 5.50, respectively.

## 2.3 Unconfined compressive strength

The unconfined compressive strength $q_u$ can be related to the mass ratios $x$ and $y$ by Chen et al.'s [2] modification of Lee et al.'s [24] and Xiao et al.'s [58] empirical relationship. This gives

$$r = \frac{q_u}{q_o} = \frac{1 + mx + (mx)^2}{(y)^n} \tag{13}$$

where $r$ is the strength ratio, and $q_0$, $m$ and $n$ are fitted parameters. By assuming that the in-situ water content of the untreated soil $w_i$ and the water-cement ratio $a$ of the cement slurry to be spatially uniform, so that the only random variable is the binder mass fraction of cement slurry $b$, Chen et al. [2] showed that the strength ratio $r$ can be expressed as

$$r = \frac{1 + m\left(\frac{1+a}{1+w_i}\right)\left(\frac{1}{b}-1\right) + \left[m\left(\frac{1+a}{1+w_i}\right)\left(\frac{1}{b}-1\right)\right]^2}{\left[w_i\left(\frac{1+a}{1+w_i}\right)\left(\frac{1}{b}-1\right) + a\right]^n} \tag{14}$$

where the binder mass fraction $b$ is defined as the mass ratio of the cement slurry to the cement-admixed clay.

Xiao et al.'s [58] values, that is $q_0$ = 13 MPa (7-day curing) and 20 MPa (28-day curing), $m$ = 0.28 and $n$ = 3,

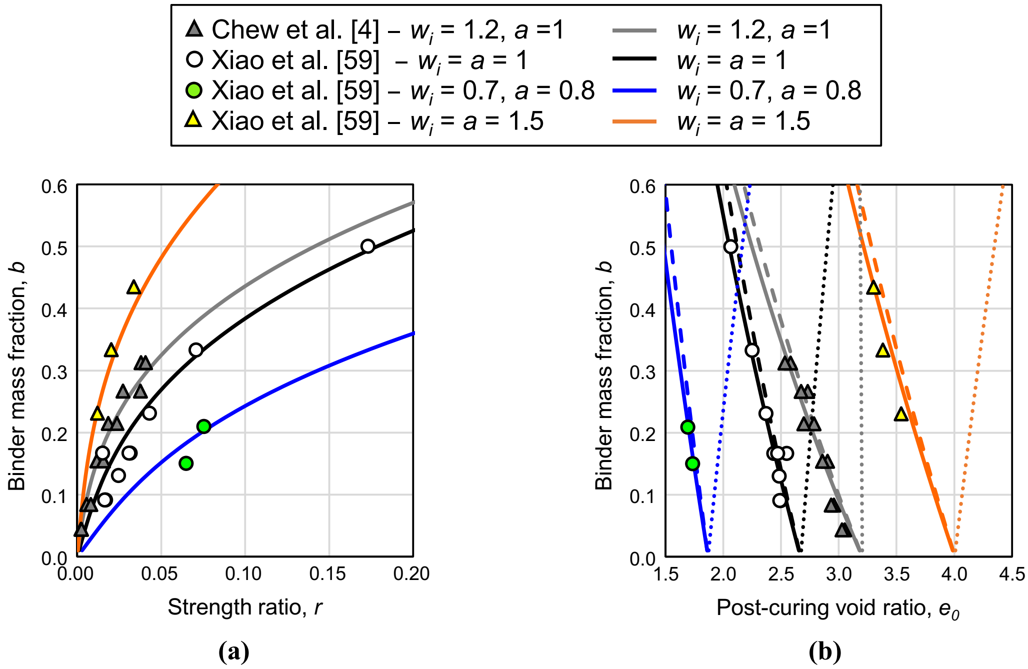


**Fig. 3** Plots of binder mass fraction $b$ versus **a** strength ratio $r$ and **b** post-curing void ratio $e_0$ for cement-admixed clays. Drained, undrained, and as-mixed void ratios are represented by dashed, bold, and dotted lines, respectively. Specific gravity of soil solids $G_s$ (Singapore marine clay) = 2.67, and specific gravity of cement powder $G_c$ (ordinary Portland cement) = 3.17

will be adopted herein. Figure 3a and b compares the strength ratio $r$ and void ratios estimated using Eqs. 3, 10, 11, and 14 with previously published values, for various combinations of $w_i$ and $a$. As seen, $e_u$ is slightly smaller than $e_d$ for the same strength ratio $r$ as the undrained assumption postulates that the capillary pores in the cement-admixed soil shrink as water is expended in the chemical reaction [50]. The estimated $e_0$-$b$ relationships correlate well with experimental data [4, 59], with $e_u$ giving slightly better agreement. This suggests that the actual curing condition may be closer to an undrained condition. Figure 3b also shows that using $e_i$ (Eq. 3) to estimate the post-curing void ratio $e_0$ will give erroneous results. The values of $e_u$ predicted using Eq. 11 will be used to estimate $e_0$ hereinafter. Combining Eqs. 11 with 12 allows the coefficient of permeability $k$ of the cement-admixed clay cured under undrained conditions to be related to its binder mass fraction $b$ by

$$\ln(k) = \frac{1}{x_1}\left[\frac{w_i\left(\frac{1+a}{1+w_i}\right)\left(\frac{1}{b}-1\right)+a-0.23h_t}{\left(\frac{1}{G_s}\right)\left(\frac{1+a}{1+w_i}\right)\left(\frac{1}{b}-1\right)+\frac{1}{G_c}+0.1716h_t}-x_2\right] \tag{15}$$

where $k$ is expressed in units of cm/s.

Combining Eqs. 14 and 15 allows the coefficient of permeability $k$ of the cement-admixed clay to be related to its strength ratio $r$ as

$$\ln(k) = \frac{1}{x_1}\left[\frac{\left[\frac{1+mx+(mx)^2}{r}\right]^{1/n}-0.23h_t}{\frac{x}{G_s}+\frac{1}{G_c}+0.1716h_t}-x_2\right] \tag{16}$$

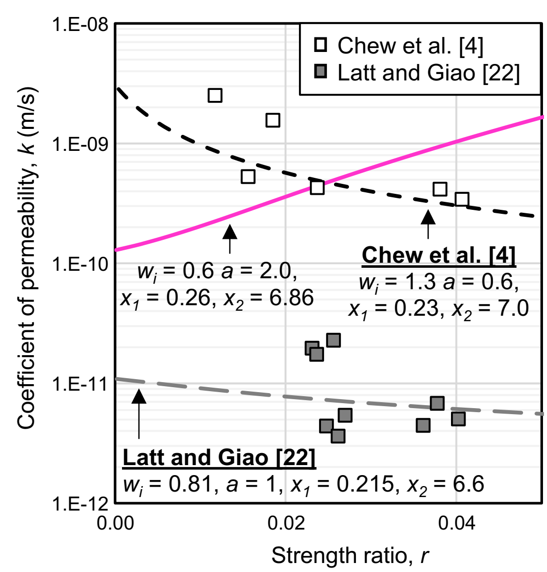


**Fig. 4** Strength ratio-permeability plot for cement-admixed clays. Experimental data are obtained from Chew et al. [4] and Latt and Giao [22]. Specific gravity of soil solids $G_s$ (Singapore marine clay and Bangkok soft clay) = 2.67, and specific gravity of cement powder $G_c$ (ordinary Portland cement) = 3.17. Assuming degree of hydration $h_t$ = 1

As Fig. 4 shows, the proposed strength ratio-permeability relationship (Eq. 16) shows good agreement with the experimental data of cement-admixed Singapore marine clay [4] and Bangkok soft clay [22]). The reduction in permeability with strength is also consistent with the observations of Xue et al. [61] and Wu et al. [57]. This is due to the increase in binder mass fraction which leads to increased strength and decrease in post-curing void ratio. Figure 4 also shows the strength ratio–permeability relationship computed based on $w_i$ of 0.60 which is the drier end of typical values for Singapore marine clays [2, 62], $a$ of 2.0 which is on the higher end range of typical values for deep mixing projects [2], and coefficients $x_1$ = 0.26 and $x_2$ = 6.86 for void ratio–permeability relationship (Eq. 12) adopted from Chew et al. [4] for cement-admixed clays. While these parameters may be atypical of field conditions encountered in deep mixing projects, the resulting strength ratio–permeability relationship can replicate the increase in treated clay permeability with strength as observed by Zhang et al. [63]. This is because untreated clays of low $w_i$ have low void ratios, which is associated with lower $k$. Subsequently, addition of cement slurry increases the strength of the mix. However, the high water-cement ratio $a$ of the cement slurry also increases the post-curing void ratio of the mix, resulting in increased $k$.

The proposed strength–permeability relationship (Eq. 16) is then coded into the finite element software GeoFEA 9 (https://www.geosoft.sg), which allows the variation in permeability to be specified as a random variable that depends on the unconfined compressive strength. The strength-permeability relationship can also

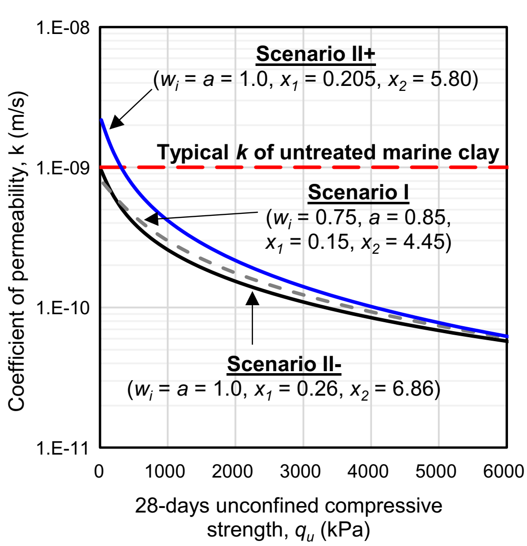


**Fig. 5** Strength-permeability plot for cement-admixed clays, using Xiao et al.'s [58] values of $q_0$ (28-days) = 20 MPa, $m$ = 0.28, and $n$ = 2.93

account for the changes in void ratio and permeability of the cement-admixed clay in consolidation problems.

## 2.4 *Scenarios I, II−, and II+*

Figure 5 shows the permeability against the 28-day strength for three scenarios, the parameters of which are summarised in Table 1. Scenario I is more representative of onshore deep mixing conditions, Table 2, whereas Scenarios II− and II+ are more representative of dredged clays stabilised using the pneumatic flow mixing method for land reclamation purposes, Table 3. In Scenario II+, coefficients $x_1$ and $x_2$ of Eq. 12 were prescribed such that a more significant change in permeability is produced for the same variation in strength than in Scenario II−. In all scenarios, the permeability decreases as strength increases, which agrees with trends reported in previous studies (e.g. [22, 42, 57]). Furthermore, when the treated clay strength approaches that of an untreated clay, the treated clay permeability approaches that of typical untreated marine clays [62]. Hence, in the limit where the binder fraction approaches zero, the permeability of the untreated clay is approximately reflected in the proposed strength–permeability relationship.

For Scenario I, using a mean binder mass fraction $b$ = 0.28 which is typical of deep-mixed columns [2], Eqs. 14 and 15 give a mean 28-day strength $q_u$ = 2100 kPa and a mean permeability $k = 1.7 \times 10^{-10}$ m/s, respectively. For Scenarios II− and II+, the mean 28-day strength is 200 kPa for a mean binder mass fraction $b$ = 0.09 corresponding to cement content $A_w$ and total water content $C_w$ of 10 and 100%, respectively, which is typical of stabilised dredged fills, Table 3, while the mean permeability $k = 1.7 \times 10^{-10}$ m/s and $1.3 \times 10^{-9}$ m/s for Scenarios II− and II+, respectively.

## 2.5 Validation

Huang et al. [14] investigated the time-dependent behaviour of a poroelastic soil subjected to axial compression using two-dimensional (2D) coupled-flow RFEM where the permeability $k$ and coefficient of volume compressibility $m_v$ were spatially variable parameters with lognormal distribution. Huang et al.'s [14] model, Fig. 6a, is re-analysed using the Cohesive Cam Clay (C3) model, Fig. 6b, incorporating randomised strength and permeability using mix design parameters from Scenario I, Table 1. Owing to spatial variation in properties, the settlement is non-uniform. Following Huang et al. [14], the average surface settlement is used to compute the average degree of consolidation $\bar{U}$, which is defined as the settlement at the respective point of time normalised by the ultimate settlement. The overall consolidation rate of each

**Table 1** Summary of parameters for the three scenarios

| Scenario | In-situ water content $w_i$ | $w/c$ ratio of cement slurry $a$ | Mean binder mass fraction $b$ | *Mean cement content $A_w$ (%) | *Mean total water content $C_w$ (%) | #Mean post-curing void ratio $e_0$ | Equation 12 $x_1$ | Equation 12 $x_2$ | ^Mean 28 days strength $q_u$ (kPa) | Mean coefficient of permeability $k$ (m/s) |
|---|---|---|---|---|---|---|---|---|---|---|
| I | 0.75 | 0.85 | 0.28 | 37 | 78 | 1.77 | 0.150 | 4.45 | 2100 | $1.7 \times 10^{-10}$ |
| II− | 1.0 | 1.0 | 0.09 | 10 | 100 | 2.55 | 0.260 | 6.86 | 200 | $6.3 \times 10^{-10}$ |
| II+ | | | | | | | 0.205 | 5.80 | | $1.3 \times 10^{-9}$ |

*Cement content $A_w$ = mass ratio of cement to soil solids, total water content $C_w$ = mass ratio of water to cement and soil solids

^ Assuming $h_t$ = 1, and Chew et al.'s [4] values of $G_s$ = 2.67 (Singapore marine clay), $G_c$ = 3.17 (ordinary Portland cement)

# Estimated using undrained curing void ratio $e_u$

**Table 2** Summary of design parameters from selected deep mixing projects

| Site | Prior to mixing | | After mixing | | | | References |
|---|---|---|---|---|---|---|---|
| | Initial water content of soft clay $w_i$ (%) | $w/c$ ratio of cement slurry $a$ | Binder mass fraction $b$ | Cement content $A_w$ (%) | Total water content $C_w$ (%) | Mean core strength $q_u$ (kPa) | |
| Marina Bay Financial Centre | 69 | 0.9 | 0.28 | 35 | 74 | 1700 | Chen et al. [2] |
| Marina One | 47 | 1.0 | 0.19 | 17 | 55 | 2100 | Liu et al. [28] |

**Table 3** Summary of design parameters from selected projects which adopted the pneumatic flow mixing method

| Project | Prior to mixing | | After mixing | | | | References |
|---|---|---|---|---|---|---|---|
| | Initial water content of dredgings $w_i$ (%) | $w/c$ ratio of cement slurry $a$ | Cement amount $C_m$ (kg/m$^3$) | *Total water-cement ratio | Cement content $A_w$ (%) | Total water content $C_w$ (%) | |
| Reclamation fill in Ishinomaki, Japan | – | – | 39–70 | 9–22 | 6–9 | 74–130 | Porbaha et al. [40] |
| Central Japan International Airport | 64–116 | 1.0 | 52–87 | 9–14 | 6–9 | 67–115 | Kitazume and Satoh [17] |
| Tokyo Haneda Airport | – | – | 85–103 | 8–10 | 15–20 | 137–140 | Watabe and Noguchi [54] |

*Total water-cement ratio of the mix is taken as mass ratio of water to cement solids

realisation is quantified by the equivalent coefficient of consolidation $c_{v,\mathrm{eq}}$, determined using the root time method [46] as such

$$c_{v,eq} = \frac{0.848(H_d)^2}{t_{90}} \tag{17}$$

where $H_d$ is the drainage path length and $t_{90}$ is the duration corresponding to 90% average degree of consolidation. The

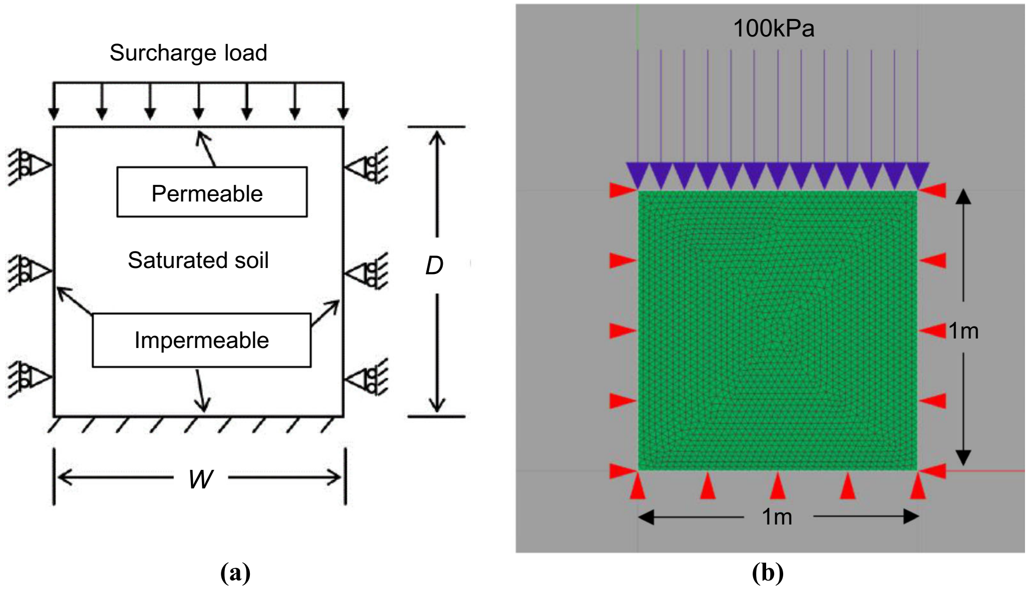


**Fig. 6** **a** Schematic of the two-dimensional (2D) problem used in validation study (after Huang et al. [14]), and **b** corresponding plane-strain finite element model. Element type: linear strain triangle, mesh size = 0.025 m

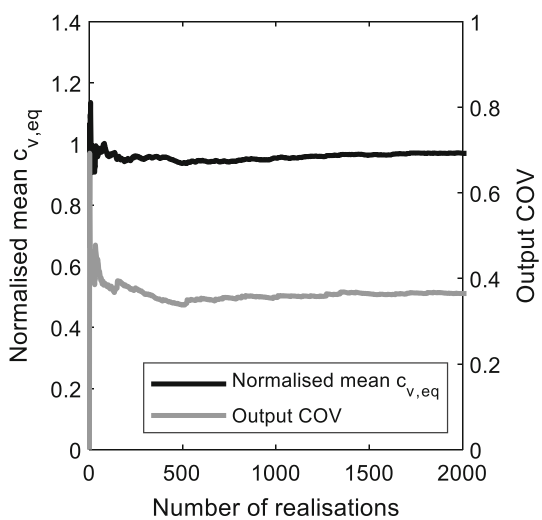


**Fig. 7** Typical convergence plot for normalised mean and COV of equivalent coefficient of consolidation $c_{v,\mathrm{eq}}$ obtained from validation study of Huang et al.'s [14] problem. Case with input COV = 0.8 and normalised SOF = 0.5 shown

mean equivalent coefficient of consolidation is obtained from 2000 realisations to ensure convergence of mean and output COV, Fig. 7. Reference cases involving uniform soil properties are also analysed; these are hereafter termed deterministic cases.

The mean values normalised by values from corresponding deterministic case, termed normalised mean hereinafter, and the coefficient of variation of equivalent coefficient of consolidation, termed output COV hereinafter, show good agreement with the results of Huang et al.'s [14], Fig. 8a and b. Due to the small magnitude of the applied load, the response of the C3 material is within its elastic region and agrees well with that of the poroelastic material used by Huang et al. [14]. However, even in its elastic regime, the C3 model is non-linear and its modulus increases with the mean effective stress [38]. This explains the minor differences between the results obtained herein and those of Huang et al. [14].

## 3 Consolidation examples

Two plane-strain consolidation examples are analysed using the software GEOFEA 9 (https://www.geosoft.sg/) which has been modified for RFEM (e.g. [9–12]). The plane-strain assumption implies that all variables are uniform in the out-of-plane direction and results obtained tend to err on the conservative side when compared to the corresponding 3D model [6, 39, 51]. As Fig. 9a shows, example 1 represents a cement-admixed clay specimen undergoing one-dimensional consolidation after an instantaneous surcharge is applied across a stiff cap at its top boundary. The top and bottom edges of the mesh are modelled as drainage boundaries, while the sides and bottom are modelled as frictionless, impermeable boundaries. Example 2 deals with a cement-admixed soil layer consolidating under uniform surcharge loading, Fig. 9b. The top surface is a drainage boundary, while the bottom and side boundaries are frictionless and impermeable. Although both examples involve one-dimensional (1D) consolidation, 2D seepage flow occurs within the soil body owing to the spatial variation in stiffness and permeability.

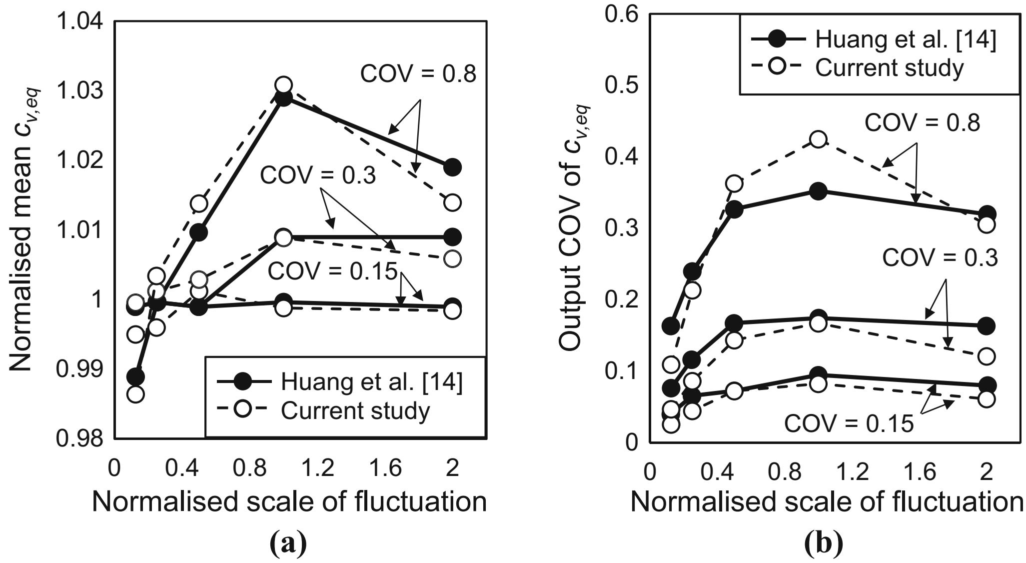


**Fig. 8** Plots of **a** normalised mean and **b** output COV of equivalent coefficient of consolidation $c_{v,\mathrm{eq}}$ against normalised SOF

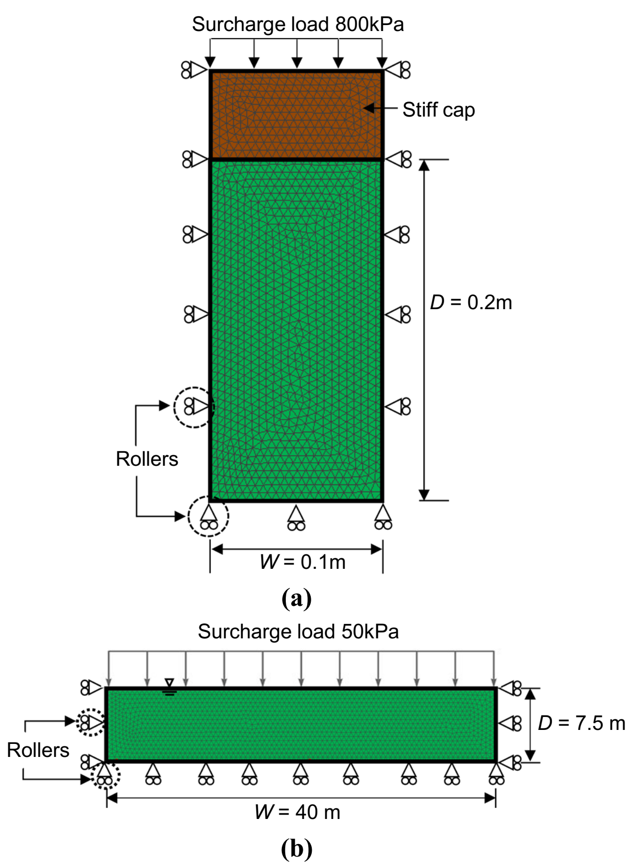


**Fig. 9** Schematic of plane-strain finite element models under 1D compression: **a** Example 1—top and bottom surfaces are free draining, average mesh size: 0.005 m; **b** Example 2—top surface is free draining, average mesh size: 0.25 m. Element type: 6-noded linear strain triangle

Example 2 is also larger in areal extent; this allows the effects of large-scale improvement to be examined.

The cement-admixed clay is modelled using Pan et al.'s [37] implementation of Xiao et al.'s [59] Cohesive Cam Clay (C3) model, with parameters shown in Table 4. The strength fitting parameters $q_o$, $m$, and $n$ of Eq. 13 are adopted from Xiao et al. [58]. Mix design parameters $w_i$, $a$, and constants $x_1$ and $x_2$ for the cement-admixed clay in examples 1 and 2 are adopted from Scenarios I and II ($-$ and $+$) in Table 1, respectively.

The statistical input parameters are the mean unconfined compressive strength $q_u$, its coefficient of variation, hereafter termed "input COV", and scale of fluctuation (SOF) [52] as well as the mean coefficient of permeability $k$. The random strength field is generated using the modified linear estimation method [26] and is assumed to follow a marginal lognormal distribution with squared exponential autocorrelation function. Other soil parameters are correlated to the soil strength.

As Table 5 shows, different random field characteristics are investigated. The RxC series involves variable strength but constant coefficient of permeability, whereas the RxV series involves variable strength and permeability. The SOF of the strength and permeability are identical as both parameters are correlated. The $\pm\, x$ and $\pm\, y$ series involves large SOF in the horizontal $x$- and vertical $y$-directions, respectively; this effectively simulates a constant value in the respective directions. Short-range SOFx may result from in-situ mixing operations where the cement-admixed soil possesses columnar structure [27, 29], whereas longer-range SOFx may result from the layered re-deposition of ex-situ stabilised dredged clays as reclamation fill (e.g.

**Table 4** Parameters for Cohesive Cam Clay (C3) material

| Parameters | $\overline{\kappa}$ | $\lambda_r$ | $M$ | $\alpha$ | $\beta$ | $\nu'$ | $V_0$ | $\sigma_t$ | $p'_{py}$ | $C_i$ |
|---|---|---|---|---|---|---|---|---|---|---|
| C3 model | 0.01 | 0.25 | 2.4 | 2.2 | 0.28 | 0.2 | $1+{}^*e_u$ | $0.13q_u$ | $0.62q_u$ | $0.36q_u$ |

*Undrained curing void ratio

**Table 5** Parametric studies in random finite element method

| Case | Input statistical characteristics | | | | Remarks | |
|---|---|---|---|---|---|---|
| | Mean strength $q_u$ (kPa) | Input strength COV | Mean coefficient of permeability $k$ (m/s) | SOFx–SOFy (m)^ of strength | | |
| R1Cx | *2100 | 0.2, 0.4, 0.6, 0.8 | *$1.7 \times 10^{-10}$ | 1000–0.04 | Scenario I | Constant $k$ |
| R1Cy | | | | 0.04–1000 | | |
| R1Cxy | | | | 0.04–0.04 | | |
| R1Vx | | | | 1000–0.04 | | Variable $k$ |
| R1Vy | | | | 0.04–1000 | | |
| R1Vxy | | | | 0.04–0.04 | | |
| R2C-x | **200 | | **$6.3 \times 10^{-10}$ | 2000–2 | Scenario II- | Constant $k$ |
| R2C-xy | | | | 2–2 | | |
| R2C-x8y4 | | | | 8–4 | | |
| R2V-x | | | | 2000–2 | | Variable $k$ |
| R2V-xy | | | | 2–2 | | |
| R2V-x8y4 | | | | 8–4 | | |
| R2C+x | | | ***$1.3 \times 10^{-9}$ | 2000–2 | Scenario II+ | Constant $k$ |
| R2C+xy | | | | 2–2 | | |
| R2C+x8y4 | | | | 8–4 | | |
| R2V+x | | | | 2000–2 | | Variable $k$ |
| R2V+xy | | | | 2–2 | | |
| R2V+x8y4 | | | | 8–4 | | |

R1 and R2 denote the randomised versions of examples 1 and 2

*Mean values obtained from Scenario I

**Mean values obtained from Scenario II−

***Mean values obtained from Scenario II+

^The former value is horizontal SOF, and the latter value is vertical SOF e.g., R2C+x: horizontal SOF is 2000 m and vertical SOF is 2 m; R2V+x8y4: horizontal SOF is 8 m, and vertical SOF is 4 m

The – and + symbols in the series identifiers indicate that the permeability-strength relation used pertain to those of Scenarios II− and II+, respectively

[18, 32, 44]). The ± $xy$ series employs an isotropic SOF. For the ± $xy$ series in Example R2, the SOFx of 2 m is adopted from Tang et al. [45]. Since less data are available for the SOFy of ex-situ stabilised dredged fills, the SOFy was assumed to be 2 m, which is larger than 0.5 m reported by Tang et al. [45]. The ± $x8y4$ series of example R2 employ SOFx and SOFy of 8 m and 4 m, respectively. This is because ex- and in-situ mixing processes are highly operator dependent and may result in larger zones of similar binder content. The SOFx is inspired from the larger end range diameters of untreated clay clumps used as reclamation fill [44], while the slightly smaller SOFy attempts to account for possible slumping upon deposition. The nominal input strength COVs of 0.4 used for the R1 and R2 series were adopted from core sample data from Liu et al. [28] and Kitazume and Satoh [18], respectively. Cases with larger COV up to 0.8 (e.g. [8]) were also analysed to study the effect of greater variability.

Following Huang et al. [14], the overall consolidation rate of each realisation was quantified by the equivalent

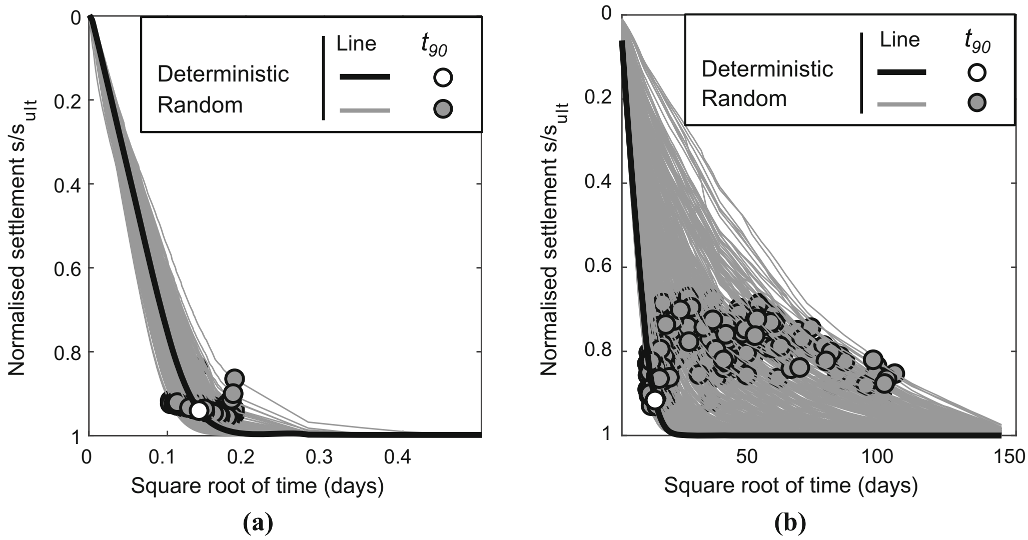


**Fig. 10** Settlement–root time curves and $t_{90}$ for deterministic and random realisations for **a** case R1C0.6y (R1 series, Scenario I, mean $q_u$ = 2100 kPa, constant permeability $k = 1.7 \times 10^{-10}$ m/s with input strength COV of 0.6, SOFx = 1000 m, SOFy = 0.04 m) and **b** case R2C-0.8xy (R2 series, Scenario II−, mean $q_u$ = 200 kPa, constant permeability $k = 6.3 \times 10^{-10}$ m/s with input strength COV of 0.8, SOFx = SOFy = 2 m). Average settlement $s$ normalised by ultimate settlement $s_{ult}$, $t_{90}$ obtained using Taylor's [46] root time method

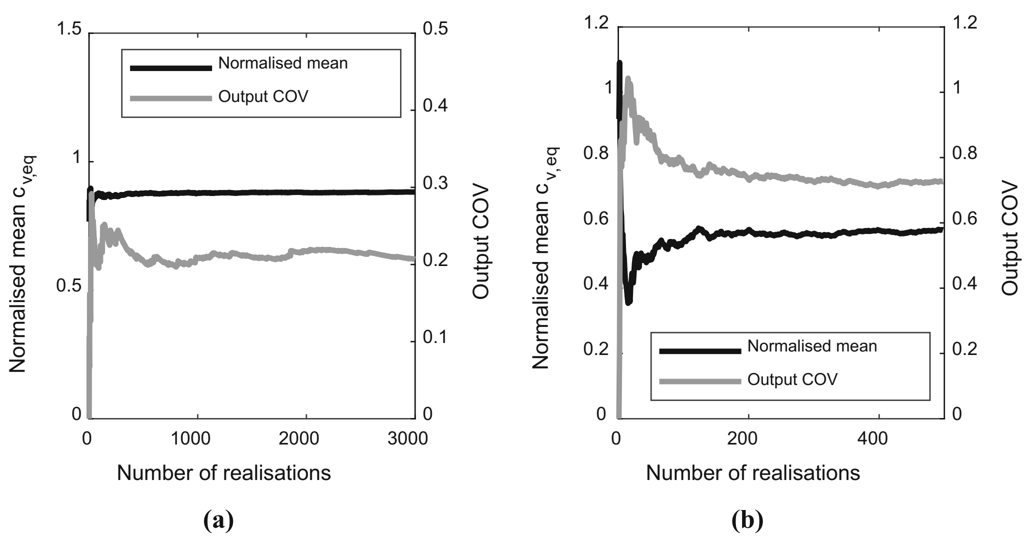


**Fig. 11** Convergence plots for normalised mean and output COV of equivalent coefficient of consolidation for **a** case R1C0.6xy (R1 series, Scenario I, mean $q_u$ = 2100 kPa, constant permeability $k = 1.7 \times 10^{-10}$ m/s with input strength COV of 0.6, SOFx = SOFy = 0.04 m), and **b** case R2C-0.8xy (R2 series, Scenario II−, mean $q_u$ = 200 kPa, constant permeability $k = 6.3 \times 10^{-10}$ m/s with input strength COV of 0.8, SOFx = SOFy = 2 m, Fig. 10b)

coefficient of consolidation $c_{v,eq}$, which was computed using the $t_{90}$ obtained from the settlement–root time curves, Fig. 10a, b. For the R1 series, the rigid cap ensures uniform surface settlement throughout consolidation. For the R2 series, the surface settlement may be non-uniform owing to spatial variability and the imposed surcharge load.

Element size effects were studied using cases R1V0.8xy and R2V + 0.8xy, which have input COVs of 0.8 and the smallest isotropic SOF, to ensure that small-scale heterogeneity can be adequately modelled by the mesh. The study shows that an element size–SOF ratio of 0.25 is sufficient to model the shortest range variation adequately for examples R1 and R2.

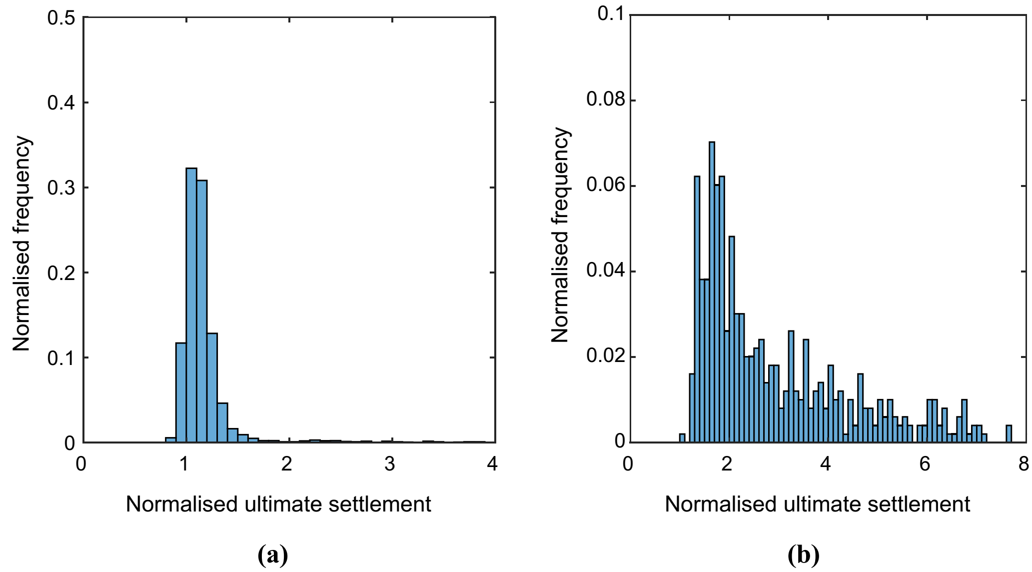


**Fig. 12** Histograms of ultimate settlement of random realisations, normalised by ultimate settlement of corresponding deterministic case, for **a** case R1C0.6xy (R1 series, Scenario I, mean $q_u$ = 2100 kPa, constant permeability $k = 1.7 \times 10^{-10}$ m/s with input strength COV of 0.6, SOFx = SOFy = 0.04 m, Fig. 11a) and **b** case R2C-0.8xy (R2 series, Scenario II−, mean $q_u$ = 200 kPa, constant permeability $k = 6.3 \times 10^{-10}$ m/s with input strength COV of 0.8, SOFx = SOFy = 2 m, Fig. 11b)

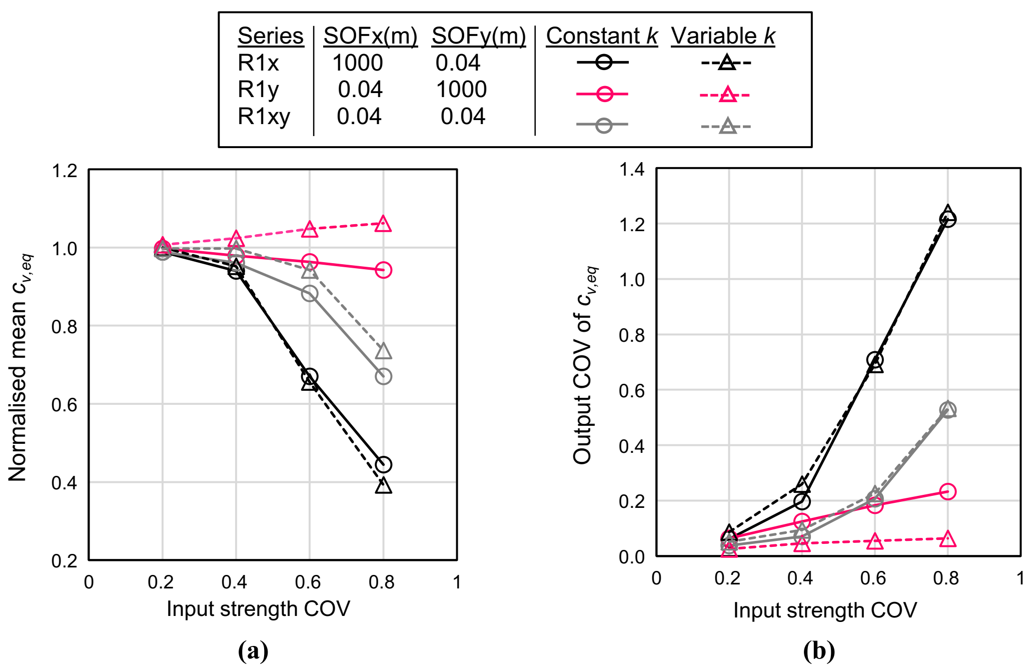


**Fig. 13** Effect of input strength COV = 0.2, 0.4, 0.6, and 0.8 on the **a** normalised mean values and **b** output COV of equivalent coefficient of consolidation $c_{v,eq}$ for R1 series (Scenario I, mean $q_u$ = 2100 kPa, mean permeability $k = 1.7 \times 10^{-10}$ m/s)

# 4 Results and discussion

## 4.1 Convergence study

As Fig. 11a, b shows, the normalised mean and COV of the $c_{v,eq}$ stabilise when the number of random realisations exceeds ~ 1000 and ~ 200 for the R1 and R2 series, respectively. The large difference in number of realisations is because the domain in series R2 is much larger than that in series R1 and therefore has greater averaging effect. At least 1500 and 300 realisations were analysed for each random case of series R1 and R2, respectively. The

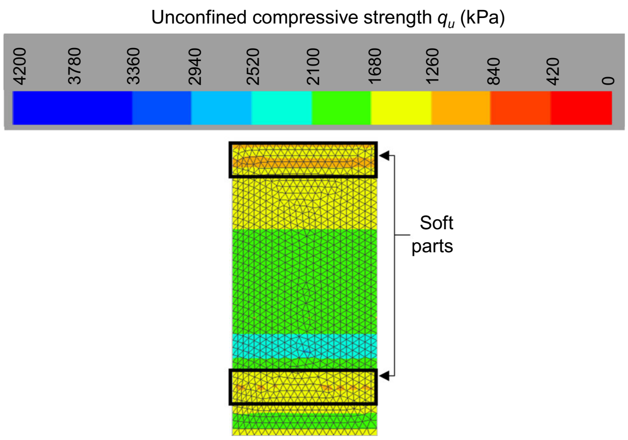


**Fig. 14** Unconfined compressive strength contour for a typical random realisation of case R1x (mean $q_u$ = 2100 kPa, mean permeability $k = 1.7 \times 10^{-10}$ m/s, SOFx = 1000 m, SOFx = 0.04 m) with input strength COV of 0.6. Soft parts with $q_u$ < 1050 kPa ($^1/_2$ the mean strength) demarcated in black

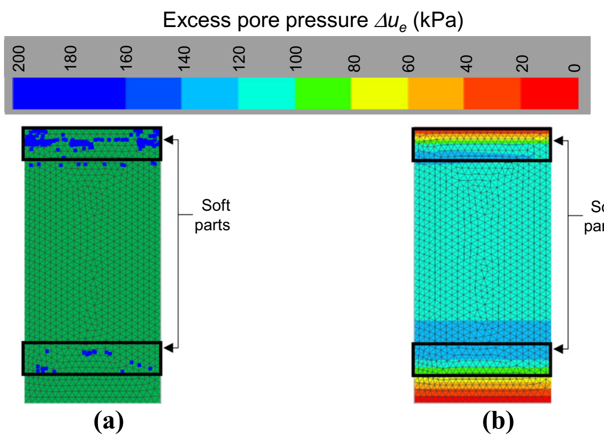


**Fig. 15** **a** Yield point contour at $t = t_{90}$ for the random realisation of case shown in Fig. 14. Yield points represented in blue. **b** Corresponding excess pore pressure contour

normalised mean values are also less than 1, Fig. 11a, b. This implies that, on average, the random realisations take longer to consolidate than the deterministic case. Owing to the presence of soft untreated zones, the random realisations also generally have larger average settlement than the deterministic realisation, Fig. 12a, b.

## 4.2 R1 series

Figure 13a, b shows the normalised mean and COV of the $c_{v,eq}$ for the R1 series, respectively. When the input strength COV is 0.4 and below, the mean values are approximately equal to that of the deterministic case, indicating that the spatial variability does not significantly affect overall consolidation behaviour. At larger input

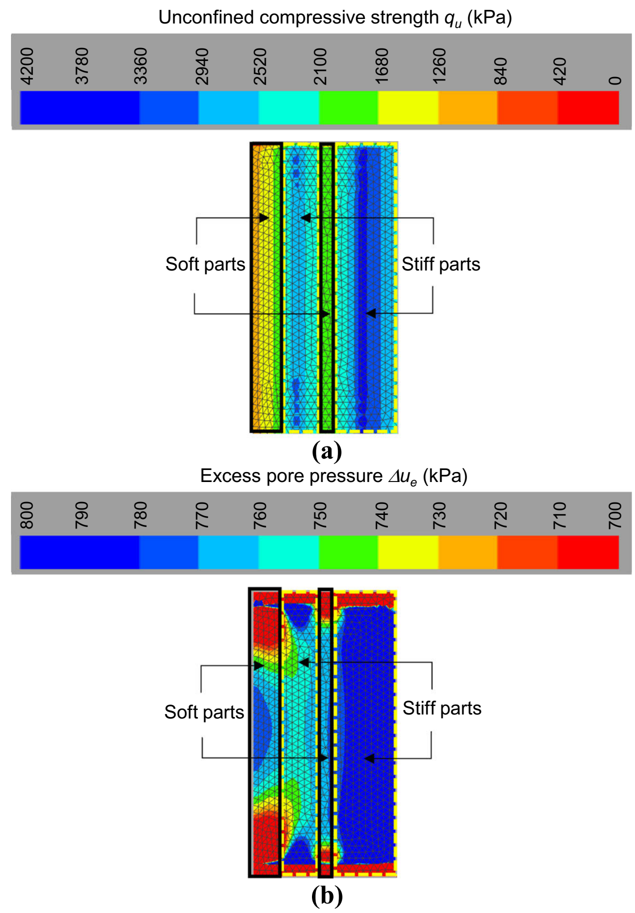


**Fig. 16** Comparison of material strength and excess pore pressure. **a** Unconfined compressive strength contour for a typical random realisation of case R1y (mean $q_u$ = 2100 kPa, mean permeability $k = 1.7 \times 10^{-10}$ m/s, SOFx = 0.04 m, SOFy = 1000 m) with input strength COV of 0.6. **b** Corresponding excess pore pressure contour at instant of loading. Soft and stiff parts demarcated in bold and dashed, respectively

COVs however, significant changes in consolidation behaviour are observed.

### 4.2.1 Effects of spatially variable permeability on horizontally layered soils

The steeper decrease in mean values for the R1x series with input strength COV, Fig. 13a, is due to the yielding of the soft parts. In the R1x series, the non-uniformities are manifested as horizontal layers, Fig. 14. The decrease in soil stiffness after yielding reduces the overall rate of consolidation. The excess pore pressure build-up in these yielded layers, Fig. 15a, impedes subsequent excess pore pressure dissipation in the inner layers, Fig. 15b, thereby generating a "soft layer screening effect". Moreover, for the variable permeability case R1Vx, the decrease in void ratio with compression results in decreased permeability, further reducing the consolidation rate as reflected in the

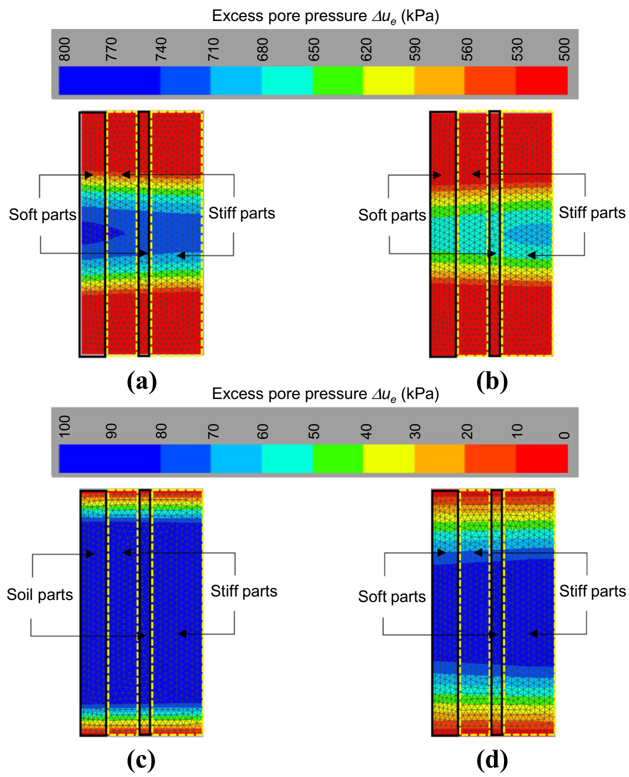


**Fig. 17** Comparison of excess pore pressure for the same random realisation with strength contour shown in Fig. 16a. Excess pore pressure contours at $t = t_{50}$ for **a** constant and **b** variable permeability realisations. Excess pore pressure contours at $t = t_{90}$ for **c** constant and **d** variable permeability realisations. Soft and stiff parts demarcated in bold and dashed, respectively

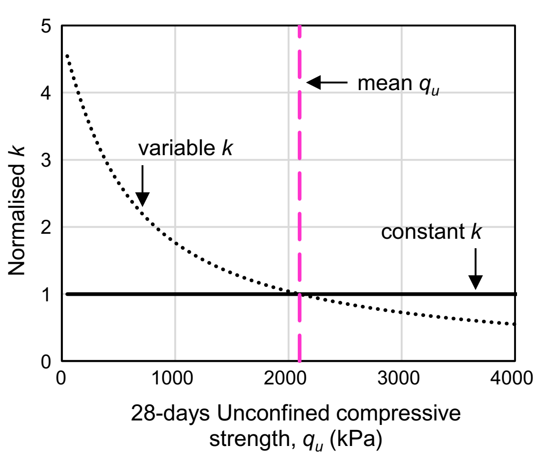


**Fig. 18** Coefficient of permeability $k$ against 28-day unconfined compressive strength $q_u$ for constant and variable permeability cases. Permeability $k$ is normalised against $1.7 \times 10^{-10}$ m/s which corresponds to the mean unconfined compressive strength (UCS) of 2100 kPa

slightly lower mean values, Fig. 13a. The large output COV for the R1x series can be attributed to the presence of

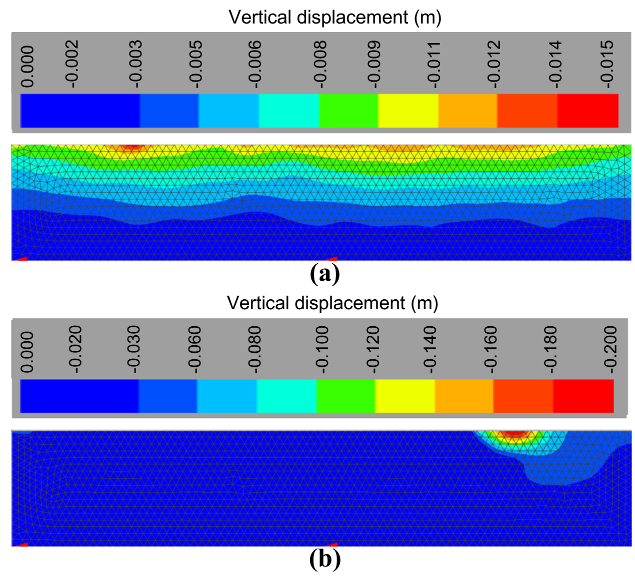


**Fig. 19** Ultimate settlement contours for a typical random realisation for case **a** R2V+0.4xy (R2 series, Scenario II+, mean $q_u$ = 200 kPa, mean permeability $k = 1.3 \times 10^{-9}$ m/s, variable permeability, SOFx = SOFy = 2 m, input strength COV of 0.4) and **b** R2V+0.4x8y4 (R2 series, Scenario II+, mean $q_u$ = 200 kPa, mean permeability $k = 1.3 \times 10^{-9}$ m/s, variable permeability, SOFx = 8 m, SOFy = 4 m, input strength COV of 0.4). Negative values indicate settlement

soft layers yielding in some realisations and not yielding in others, Fig. 13b.

#### 4.2.2 Effects of spatially variable permeability on vertically panelled soils

For the R1y series, the heterogeneity takes the form of vertical panels, Fig. 16a. Upon load application, the loading is concentrated onto the stiffer panel(s). Thus, the excess pore pressure distribution is also panel-like, Fig. 16b. The ground's ability to redistribute load decreases the likelihood of soft part yielding, as reflected in the larger mean values, Fig. 13a.

To investigate the effect of spatially variable permeability, a typical random realisation of case R1y is examined, Fig. 16a, b. The stiffer panels in the constant permeability case R1Cy facilitate excess pore pressure dissipation in the softer adjacent panels, Fig. 17a. For the variable permeability realisation R1Vy, the softer panels are more permeable, while the stiffer panels are less permeable, Fig. 18. These softer panels act as permeable channels to hasten the dissipation of excess pore pressure in the stiffer, more impermeable panels, Fig. 17b, resulting in larger overall consolidation rates, Fig. 17d. Thus, the overall consolidation rate for the constant permeability case R1Cy is dominated by the slower response of the

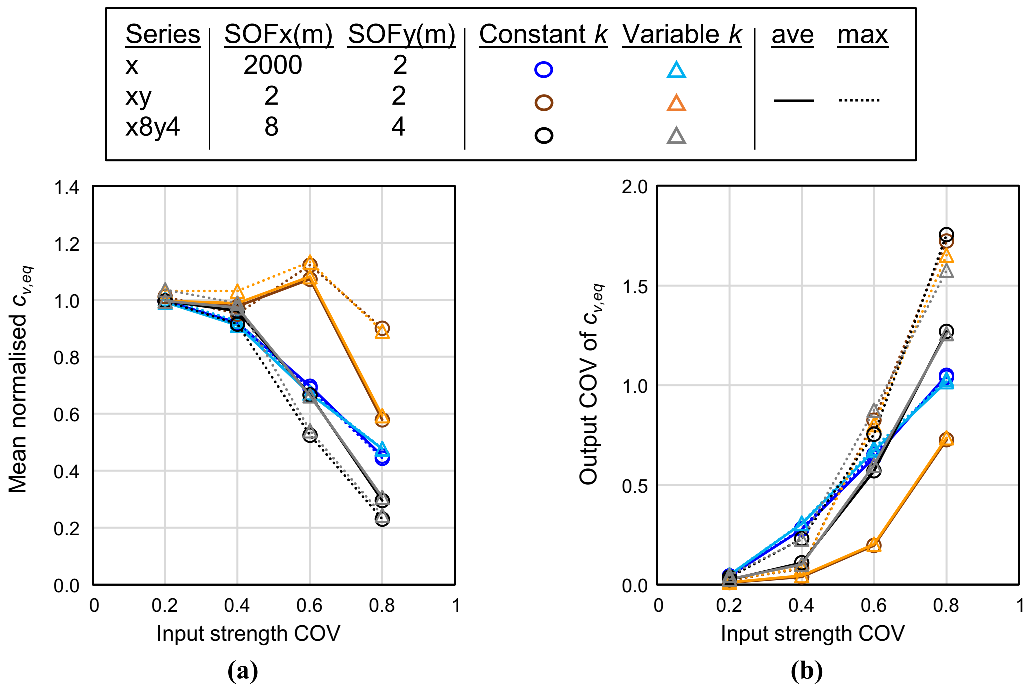


**Fig. 20** **a** Normalised mean and **b** output COV of equivalent coefficient of consolidation against input strength COV = 0.2, 0.4, 0.6, and 0.8 for R2- series (Scenario II−, mean $q_u$ = 200 kPa, mean permeability $k = 6.3 \times 10^{-10}$ m/s). Values computed using average and maximum settlement criteria are denoted as ave (bold lines) and max (dashed lines), respectively

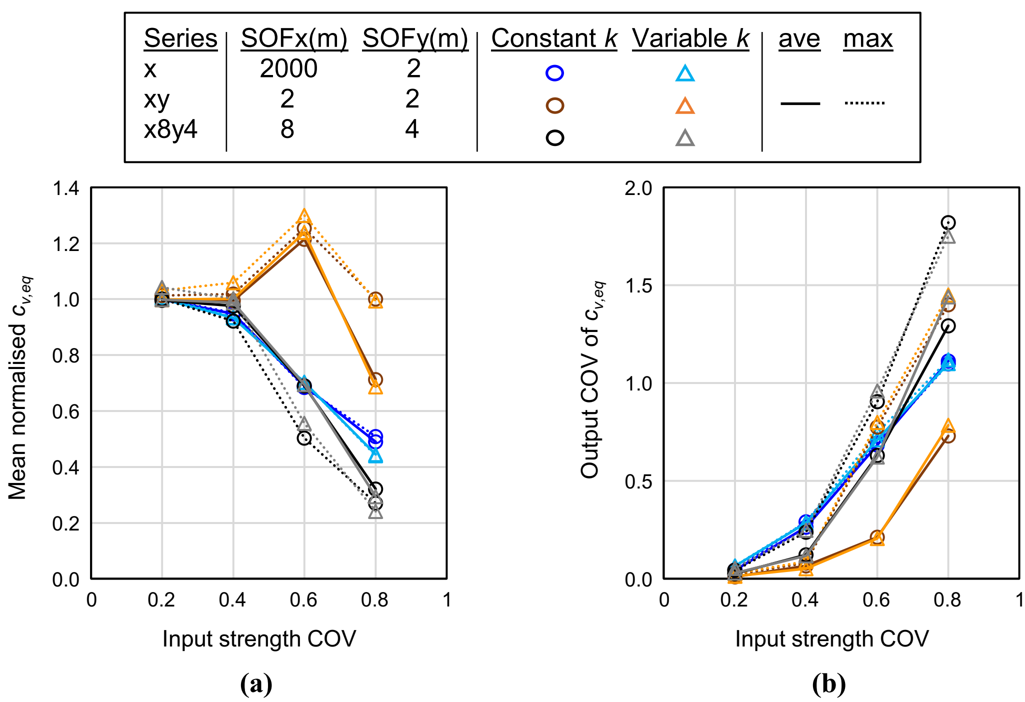


**Fig. 21** **a** Normalised mean and **b** output COV of equivalent coefficient of consolidation against input strength COV = 0.2, 0.4, 0.6, and 0.8 for R2+ series (Scenario II+, mean $q_u$ = 200 kPa, mean permeability $k = 1.3 \times 10^{-9}$ m/s). Values computed using average and maximum settlement criteria are denoted as ave (bold lines) and max (dashed lines), respectively

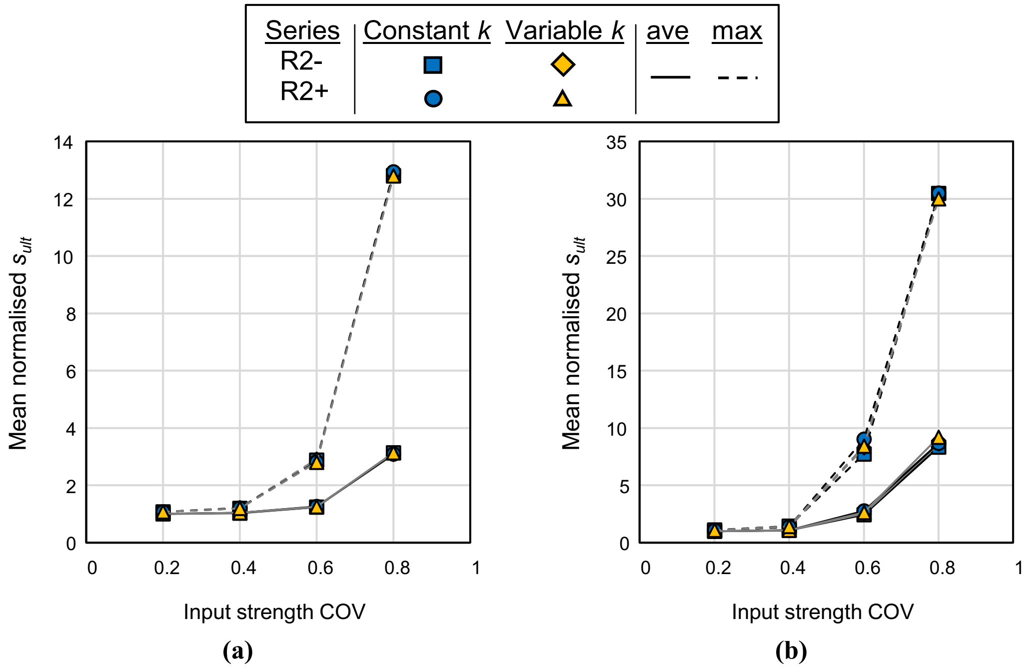


**Fig. 22** Effect of input strength COV = 0.2, 0.4, 0.6, and 0.8 on normalised mean ultimate settlement $s_{\mathrm{ult}}$ for series **a** R2xy (SOFx = SOFy = 2 m) and **b** R2x8y4 (SOFx = 8 m, SOFy = 4 m)

softer panels, while the overall consolidation rate for the variable permeability series R1Vy is dominated by the consolidation response of the less permeable, stiffer panels. This explains the consistently higher mean and lower output COV values for the variable permeability series R1Vy, Fig. 13a, b.

#### 4.2.3 Effects of spatially variable permeability on clustered soils

For the R1xy series, the SOF in the *x*- and *y*-directions are equal and smaller than the dimensions of the problem. Thus, the overall consolidation rate is highly dependent on whether load distribution can occur. As Fig. 13a, b shows, the normalised mean and output COV values lie between those of the two extreme random alignments discussed above.

### 4.3 R2 series

#### 4.3.1 Comparison between average and maximum settlement criteria

The surface settlement observed in the R2 series is non-uniform, Fig. 19a, b. Thus, using the average settlement alone to quantify the progress of consolidation may obscure important information and trends. To augment this, the settlement of the node with the maximum ultimate settlement is also used to estimate the equivalent $c_v$. As Figs. 20 and 21 show, using the average and maximum settlement to compute the mean and output COV for the R2x series give similar results since heterogeneity is manifested as horizontal layers.

For the R2xy series, the mean and output COV computed using the maximum settlement is significantly larger than that using average settlement, particularly for larger input strength COVs, Figs. 20 and 21. This is because in many realisations, the surface soft parts undergo the same ultimate settlement but return a higher equivalent coefficient of consolidation due to shorter drainage paths. The domain averaging effects [52] also become more significant with input strength COV, resulting in larger differences in maximum and average ultimate settlement, Fig. 22a.

For the R2x8y4 series, the average settlement gives larger mean values than the maximum settlement, Figs. 20a and 21a. This is because locations with maximum settlement correspond to the largest soft cluster. This soft cluster consolidates slowly upon yielding, giving a low localised equivalent $c_v$, whereas the adjacent stiffer parts can help increase the overall consolidation rate based on average settlement. Drainage paths of larger soft clusters are more similar regardless of location, as seen in the smaller difference between mean values obtained from the average

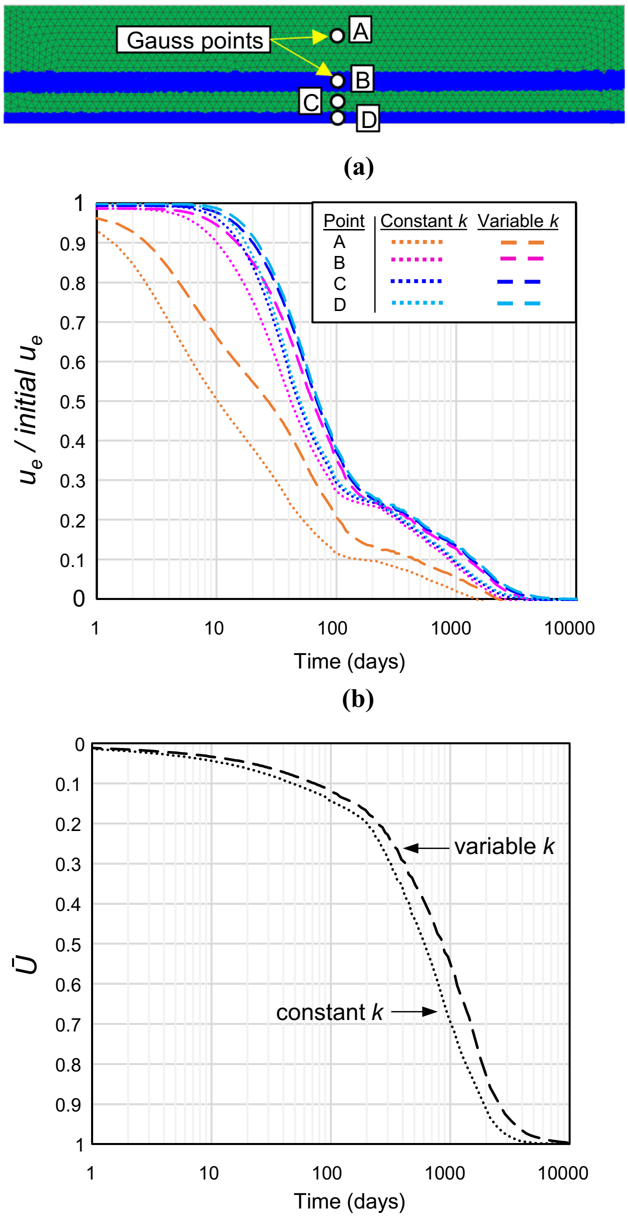


**Fig. 23** **a** Ultimate yield point contour for a typical random realisation of the R2x case with input strength COV of 0.8. Yielded layers represented in blue. Plots of **b** excess pore pressure $u_e$ normalised against initial excess pore pressure and **c** average degree of consolidation $\overline{U}$ with time. Excess pore pressure extracted from Gauss points A, B, C, and D

and maximum settlement, Figs. 20a and 21a. Nevertheless, local averaging effects [52] are significant, especially at larger input strength COVs, Fig. 22b.

Increased local averaging with input strength COV also results in larger differences in output COV between the average and maximum settlement criteria, Figs. 20b and 21b. Thus, using the maximum settlement criterion to predict overall consolidation rate can be misleading. The average settlement criterion is the more reliable representation of the overall consolidation rate and is adopted herein.

#### 4.3.2 Mean and output COV

The mean equivalent $c_v$ for the R2 series remains similar to the deterministic case when input strength COV is small, Figs. 20a and 21a. As input strength COV increases, the mean values generally reduce and at different rates for series R2x, R2xy, and R2x8y4. Similarly, the output COV increment with input COV is SOF dependent, Figs. 20b and 21b.

#### 4.3.3 Effects of spatially variable permeability on horizontally layered soils

As in the R1x series, the mean equivalent $c_v$ for the R2x series decreases with input COV, Figs. 20a and 21a. A typical random realisation of series R2x is examined to investigate the time-dependent pore pressure dissipation in layers of different strengths. Excess pore pressures were monitored at points A to D, Fig. 23a. Figure 23b shows the excess pore pressure dissipation with time of these four points, normalised by the initial induced excess pore pressure. As seen, excess pore pressure stagnation occurs after ~ 150 days despite on-going surface settlement, Fig. 23c. The decrease in stiffness of the softer layers after yielding causes excess pore pressure build-up in the inner layers, retarding subsequent excess pore pressure dissipation. This reduces the overall consolidation rate, thereby generating a "soft layer screening effect". This soft layer screening effect may also explain the excess pore pressure stagnation in the consolidating marine clay under surcharge loads observed in the Changi Airport reclamation works [7, 25, 43]. Throughout consolidation, the variable permeability realisation consistently manifests slower excess pore pressure dissipation and overall consolidation rate, Fig. 23b and c, respectively. This can be attributed to the lower initial permeability of the stiff overlying layers; permeability of the soil layer located near the drainage boundary affects the overall consolidation behaviour more than that of the underlying layers. This is further accentuated by the reduction in permeability of the treated ground with compression for the variable permeability case.

Figure 23b and c also show that using the excess pore pressure to estimate the time-dependent settlement of heterogeneous soils can give erroneous predictions, as noted by Pyrah [41] and Huang et al. [14]. In most cases, the constant and variable permeability cases of the R2x series show similar mean values and output COVs, Figs. 20 and 21. This suggests that the effect of variable permeability is neutralised by the equal number of realisations with stiffer and softer overlying layers.

#### 4.3.4 Effects of spatially variable permeability on clustered soils

For the R2xy and R2x8y4 series, spatially variable permeability has less significance on the mean equivalent $c_v$ as compared to the R1xy series, Figs. 20a and 21a. This is due to two reasons. Firstly, the R2 series have smaller variations in strength and permeability than the R1 series. This is due to the lower mean strength used in the former, Table 5. Secondly, the larger width-to-horizontal SOF ratio (*W*/SOFx) in the R2xy and R2x8y4 series results in a more homogenised overall consolidation rate due to increased local averaging. The larger W/SOFx in the R2xy series also introduces soil arching effects [13, 19, 48, 60], where the applied stresses are redistributed onto the stiffer parts that extend across the depth of the layer. The softer parts experience less stresses which reduces the likelihood of forming yielded zones, thus resulting in an increase in mean equivalent $c_v$ when the input strength COV increases to 0.6, Figs. 20a and 21a. However, when the input COV increases to 0.8, the low yield strengths of the soft clusters are exceeded despite load redistribution, leading to a steep reduction in the mean values. Thus, the input strength COV has an important impact on the mean values.

The R2xy series have larger mean equivalent $c_v$ than the R2x and R2x8y4 series, Figs. 20a and 21a. The output COV of the R2xy series is also lower, Figs. 20b and 21b. This is due to the larger averaging effect of using the average settlement for the R2xy series. Moreover, in the R2x series, yielded horizontal layers cause blanket blockages spanning across the entire improved soil width since all draining excess pore water must permeate through these horizontal layers. Similar observations were noted by Huang et al. [14], who reported that low permeability elements caused blanket blockages for the one-dimensional (1D) consolidation cases. On the other hand, in addition to soil arching, blockages in the R2xy series are more localised and only affect the global consolidation rates at higher input COVs.

Despite local averaging, the mean and output COV values for the R2x8y4 series are closer to that of the R2x series than to the R2xy series. Like in the R2x series, the large overlying clusters in series R2x8y4 also present as blanket blockages. Moreover, upon yielding, thicker clusters require longer consolidation durations, which explains the smaller mean values of the R2x8y4 series at large input strength COVs.

## 5 Conclusion

In the foregoing discussion, a framework for relating the unconfined compressive strength of cement-admixed clays to its permeability is proposed. The correlations of coefficient of permeability with strength of the cement-admixed clay are based on the notion that both are related to the binder content in the mix. The results show that the effect of spatially variable permeability on the overall consolidation rate depends largely on the scale of fluctuation configuration. For cases where load redistribution is permitted and yielding is less likely to occur, the uniform and spatially variable permeability cases exhibit different mechanisms and trends in overall consolidation behaviour, which is further exacerbated with increased strength variability. This may be crucial when estimating the consolidation settlement of soil masses such as embankments stabilised using in-situ deep mixing methods [64]. However, for cases where the soft parts yield, the stiffness reduction of the yielded soils causes excess pore pressure stagnation in the inner soils, thereby dominating the overall consolidation rate. Thus, the effect of spatially variable permeability, which also accounts for the reduction in soil permeability after yielding, becomes less significant across all input strength COVs. Increased strength variability also generally led to lower mean and increased variability in the overall consolidation rates.

The approach shows that the random variation in permeability in cement-admixed soil can be considered in a rational manner based on first principles, which may better predict the settlement of cement-admixed clays undergoing 1D consolidation. Although the focus of this study is on cement-admixed clays, it may be applied to assess the final permeability of cement-admixed sands [55], where the variation in permeability with binder content is likely to be even greater. This is likely to be crucial, for instance, in scenarios where overlapping cement-admixed sand columns are used as seepage cut-off walls in locations with permeable soil and high groundwater table.

**Acknowledgements** This research was supported by the National University of Singapore Research Scholarship.

**Funding** Open access funding provided by NTNU Norwegian University of Science and Technology (incl St. Olavs Hospital - Trondheim University Hospital). This research was supported by the National University of Singapore Research Scholarship.

**Availability of data and materials** Not applicable.

**Code availability** Not applicable.

## Declarations

**Conflict of interest** Not applicable.

## References

1. Bari MW, Shahin MA (2015) Three-dimensional finite element analysis of spatially variable PVD improved ground. GeoRisk Assess Manag Risk Eng Syst Geohazards 9(1):37–48
2. Chen EJ, Liu Y, Lee FH (2016) A statistical model for the unconfined compressive strength of deep-mixed columns. Géotechnique 66(5):351–365
3. Cheng Y, Zhang LL, Li JH, Zhang LM, Wang JH, Wang DY (2017) Consolidation in spatially random unsaturated soils based on coupled flow-deformation simulation. Int J Numer Anal Methods Geomech 41(5):682–706
4. Chew SH, Kamruzzaman AHM, Lee FH (2004) Physicochemical and engineering behavior of cement treated clays. J Geotech Geoenviron Eng 130(7):696–706
5. Chin KG (2006) Constitutive behaviour of cement treated marine clay. Doctoral dissertation, National University of Singapore, Singapore
6. Ching J, Lee SW, Phoon KK (2016) Undrained strength for a 3D spatially variable clay column subjected to compression or shear. Probab Eng Mech 45:127–139
7. Choa V, Karunaratne G, Ramaswamy S, Vijiaratnam A, Lee SW (1981) Drain performance in Changi marine clay. In: Proceedings of the 10th international conference on soil mechanics and foundation engineering, vol 3, Stockholm
8. Filz GM, Navin MP (2006) Stability of column-supported embankments. Virginia Center for Transportation Innovation and Research
9. Griffiths DV, Fenton GA, Manoharan N (2002) Bearing capacity of rough rigid strip footing on cohesive soil: probabilistic study. J Geotech Geoenviron Eng 128(9):743–755
10. Griffiths DV, Fenton GA (2004) Probabilistic slope stability analysis by finite elements. J Geotech Geoenviron Eng 130(5):507–518
11. Griffiths DV, Fenton GA, Ziemann HR (2006) Seeking out failure: the random finite element method (RFEM) in probabilistic geotechnical analysis. In: GeoCongress 2006: geotechnical engineering in the information technology age, pp 1–6
12. Griffiths DV, Fenton GA (eds) (2007) Probabilistic methods in geotechnical engineering, vol 491. Springer, New York
13. Han J, Wang F, Al-Naddaf M, Xu C (2017) Progressive development of two-dimensional soil arching with displacement. Int J Geomech 17(12):04017112
14. Huang J, Griffiths DV, Fenton GA (2010) Probabilistic analysis of coupled soil consolidation. J Geotech Geoenviron Eng 136(3):417–430
15. Jamsawang P, Voottipruex P, Tanseng P, Jongpradist P, Bergado DT (2019) Effectiveness of deep cement mixing walls with top-down construction for deep excavations in soft clay: case study and 3D simulation. Acta Geotech 14(1):225–246
16. Kamruzzaman AH, Chew SH, Lee FH (2009) Structuration and destructuration behavior of cement-treated Singapore marine clay. J Geotech Geoenviron Eng 135(4):573–589
17. Kitazume M, Satoh T (2003) Development of a pneumatic flow mixing method and its application to Central Japan International Airport construction. Proc Inst Civ Eng Ground Improv 7(3):139–148
18. Kitazume M, Satoh T (2005) Quality control in central Japan international airport construction. Proc Inst Civ Eng Ground Improv 9(2):59–66
19. Lai HJ, Zheng JJ, Cui MJ, Chu J (2020) "Soil arching" for piled embankments: insights from stress redistribution behaviour of DEM modelling. Acta Geotech 15(8):2117–2136
20. Larsson S, Stille H, Olsson L (2005) On horizontal variability in lime-cement columns in deep mixing. Géotechnique 55(1):33–44
21. Larsson S, Nilsson A (2009) Horizontal strength variability in lime-cement columns. In: Deep mixing 2009 Okinawa symposium, DM' 09. Okinawa, Japan. 19–21 May 2009. SANWA CO., LTD, pp 629–634
22. Latt KM, Giao PH (2017) Prediction of permeability of cement-admixed soft clay using resistivity and time-domain IP measurements. J Appl Geophys 137:92–103
23. Lee FH, Yong KY, Quan KC, Chee KT (1998) Effect of corners in strutted excavations: field monitoring and case histories. J Geotech Geoenviron Eng 124(4):339–349
24. Lee FH, Lee Y, Chew SH, Yong KY (2005) Strength and modulus of marine clay-cement mixes. J Geotech Geoenviron Eng 131(2):178–186
25. Lee SL, Tan SA, Karunaratne GP, Chan V (1990) Consolidation of clays in Changi Airport pilot test. Geotech Eng 21:3–30
26. Liu Y, Lee FH, Quek ST, Beer M (2014) Modified linear estimation method for generating multi-dimensional multi-variate Gaussian field in modelling material properties. Probab Eng Mech 38:42–53
27. Liu Y, Lee FH, Quek ST, Chen EJ, Yi JT (2015) Effect of spatial variation of strength and modulus on the lateral compression response of cement-admixed clay slab. Géotechnique 65(10):851–865
28. Liu Y, Jiang YJ, Xiao H, Lee FH (2017) Determination of representative strength of deep cement-mixed clay from core strength data. Géotechnique 67(4):350–364
29. Liu Y, He LQ, Jiang YJ, Sun MM, Chen EJ, Lee FH (2019) Effect of in situ water content variation on the spatial variation of strength of deep cement-mixed clay. Géotechnique 69(5):391–405
30. Lorenzo GA, Bergado DT (2004) Fundamental parameters of cement-admixed clay—new approach. J Geotech Geoenviron Eng 130(10):1042–1050
31. Lorenzo GA, Bergado DT (2006) Fundamental characteristics of cement-admixed clay in deep mixing. J Mater Civ Eng 18(2):161–174
32. Morohoshi K, Yoshinaga K, Miyata M, Sasaki I, Saitoh H, Tokoro M, Ishikawa M (2010) Design and long-term monitoring of Tokyo International Airport extension project constructed on super-soft ground. Geotech Geol Eng 28(3):223–232
33. Namikawa T, Koseki J (2013) Effects of spatial correlation on the compression behavior of a cement-treated column. J Geotech Geoenviron Eng 139(8):1346–1359
34. Neville AM (1995) Properties of concrete, vol 4. Longman, London
35. Onitsuka K, Modmoltin C, Kouno M, Negami T (2003) Effect of organic matter on lime and cement stabilized Ariake clays. Doboku Gakkai Ronbunshu 2003(729):1–13
36. O'Rourke TD, McGinn AJ (2004) Case history of deep mixing soil stabilization for Boston Central artery. In: Geotechnical engineering for transportation projects, pp 77–136

37. Pan Y, Liu Y, Xiao H, Lee FH, Phoon KK (2018) Effect of spatial variability on short-and long-term behaviour of axially-loaded cement-admixed marine clay column. Comput Geotech 94:150–168
38. Pan Y, Liu Y, Lee FH, Phoon KK (2019) Analysis of cement-treated soil slab for deep excavation support—a rational approach. Géotechnique 69(10):888–905. https://doi.org/10.1680/jgeot.18.P.002
39. Pan Y, Liu Y, Tyagi A, Lee FH, Li DQ (2020) Model-independent strength-reduction factor for effect of spatial variability on tunnel with improved soil surrounds. Géotechnique. https://doi.org/10.1680/jgeot.19.P.056
40. Porbaha A, Hanzawa H, Shima M (1999) Technology of air-transported stabilized dredged fill. Part 1: pilot study. Proc Inst Civ Eng Ground Improv 3(2):49–58
41. Pyrah IC (1996) One-dimensional consolidation of layered soils. Geotechnique 46(3):555–560
42. Quang ND, Chai JC (2015) Permeability of lime-and cement-treated clayey soils. Can Geotech J 52(9):1221–1227
43. Tan SA, Lee SL, Karunaratne GP, Choa V (1987) Design of drains and surcharge in reclamations. Soils Found 27(4):89–98
44. Tan TS, Lu YT, Phoon KK, Karthikeyan M (2011) Innovative approaches to land reclamation in Singapore. In: Proceedings of advances in ground technology and geo-information, pp 85–102
45. Tang YX, Miyazaki Y, Tsuchida T (2001) Practices of reused dredgings by cement treatment. Soils Found 41(5):129–143
46. Taylor DW (1948) Fundamentals of soil mechanics, vol 66, no 2, p 161. LWW
47. Terashi M, Tanaka H (1983) Settlement analysis for deep mixing method. In: Proceedings of the 8th European conference on soil mechanics and foundation engineering, vol 2, pp 955–960
48. Terzaghi K (1943) Theoretical soil mechanics. Wiley, New York, pp 11–15
49. Three runway-system (2017) Hong Kong International Airport Master Plan 2030—technical report. Accessed 2 Aug 2019. https://www.threerunwaysystem.com/media/1296/meindhart_1.pdf
50. Tyagi A, Xiao H, Chin KG, Lee FH (2019) Model for predicting the unit weight of cement-treated soils. Soils Found 59:1921–1932
51. Tyagi A, Liu Y, Pan YT, Lee FH (2020) Equivalent strength for tunnels in cement-admixed soil columns with spatial variability and positioning error. J Geotech Geoenviron Eng 146(10):04020101
52. Vanmarcke E (1983) Random fields: analysis and synthesis
53. Vitale E, Deneele D, Russo G, De Sarno D, Nicotera MV, Papa R, Urciuoli G (2020) Chemo-mechanical behaviour of lightweight cemented soils. Acta Geotech 15(4):933–945
54. Watabe Y, Noguchi T (2011) Site-investigation and geotechnical design of D-runway construction in Tokyo Haneda Airport. Soils Found 51(6):1003–1018
55. Wei X, Ku T (2020) New design chart for geotechnical ground improvement: characterizing cement-stabilized sand. Acta Geotech 15(4):999–1011
56. Wei X, Liu H, Ku T (2020) Microscale analysis to characterize effects of water content on the strength of cement-stabilized sand–clay mixtures. Acta Geotech 15(10):2905–2923
57. Wu J, Deng Y, Zheng X, Cui Y, Zhao Z, Chen Y, Zha F (2019) Hydraulic conductivity and strength of foamed cement-stabilized marine clay. Constr Build Mater 222:688–698
58. Xiao H, Lee FH, Chin KG (2014) Yielding of cement-treated marine clay. Soils Found 54(3):488–501
59. Xiao H, Lee FH, Liu Y (2016) Bounding surface cam-clay model with cohesion for cement-admixed clay. Int J Geomech 17(1):04016026
60. Xu C, Liang L, Chen Q, Luo W, Chen YF (2019) Experimental study of soil arching effect under seepage condition. Acta Geotech 14(6):2031–2044
61. Xue Q, Li JS, Liu L (2013) Experimental study on anti-seepage grout made of leachate contaminated clay in landfill. Appl Clay Sci 80:438–442
62. Yong KY, Karunaratne GP, Lee SL (1990) Recent developments in soft clay engineering in Singapore. In: Kansai International Geotech Forum '90, Osaka, Japan, pp 1–8
63. Zhang C, Yang J, Ou X, Fu J, Xie Y, Liang X (2018) Clay dosage and water/cement ratio of clay-cement grout for optimal engineering performance. Appl Clay Sci 163:312–318
64. Zhang Z, Rao FR, Ye GB (2019) Design method for calculating settlement of stiffened deep mixed column-supported embankment over soft clay. Acta Geotech 55:1–20